Polymer Testing 156 (2026) 109120

Contents lists available at ScienceDirect

Polymer Testing

journal homepage: www.elsevier.com/locate/polytest

Modeling the morphology evolution of PET during equi-biaxial elongation: from SAXS measurement to viscoelastic behavior prediction

Luc Chevalier *, Yun-Mei Luo

Université Gustave Eiffel, Laboratoire Modélisation et Simulation Multi Echelle, MSME UMR 8208 CNRS, Marne-la-Vallée, 77454, France

A B S T R A C T

The microstructure induced by the biaxial stretching of PET under conditions representative of the stretch blow-molding process enhances the material's mechanical performance. Using equi-biaxial tensile tests combined with small-angle synchrotron scattering, the evolution of the deformation-induced microstructure can be monitored in situ. This approach enables the characterization of the size and morphology of the crystalline phase, as well as the evolution of the degree of crystallinity during stretching.

A constitutive model accounting for this microstructural evolution, based on a double homogenization of the viscoelastic behavior of the amorphous phase and the quasi-elastic response of the crystalline phase, successfully reproduces the macroscopic mechanical behavior of PET, including its characteristic strain-hardening during elongation. This modeling framework represents a significant advancement and provides a basis for extending the approach to other biaxiality ratios encountered in industrial stretch blow-molding processes.

1. Introduction

The evolution of microstructure plays a decisive role in determining the properties induced by uniaxial or biaxial stretching of polymers. As shown by Luo et al. [1], a detailed representation of the spherulitic microstructure enables accurate prediction of the elastic properties of polyethylene terephthalate (PET) through mechanical homogenization. In the case of PET stretch blow-molding, heating slightly above the glass transition temperature (*Tg*) combined with high biaxial stretch ratios significantly enhances the mechanical performance of bottles. This strengthening effect, first reported several decades ago (see Chevalier et al. [2]), has been consistently confirmed by various experimental methods and measurement techniques [3–10].

Understanding the evolution of microstructure in order to deduce the resulting material properties has remained a key research objective since the early 2000s. Early studies, such as that of Prevorsek et al. [11], had already proposed microstructural models composed of crystalline lamellae connected by oriented amorphous regions. A major step forward came in 1999 with the work of Mahendrasingam et al. [12], who conducted and analyzed the first in situ uniaxial tensile tests under X-ray beams, providing key insights into the thermomechanical conditions leading to crystallization. Following this pioneering work, several authors, including Marco et al. [13,14], Kawakami et al. [15], Okada et al. [16], and more recently Quandalle [17], have performed in situ uniaxial tensile experiments coupled with Wide-Angle X-ray Scattering (WAXS) or Small-Angle X-ray Scattering (SAXS) measurements under various strain rates and temperature conditions. In addition, numerous *post-mortem* analyses have been carried out on pre-stretched biaxial specimens or on samples extracted from blown bottles to characterize the induced microstructure. To the best of our knowledge, although several in-situ biaxial stretching setups have recently been developed for synchrotron applications [18,19], investigations combining in-situ X-ray characterization with biaxial tensile deformation of PET remain limited [20–22], particularly under large strain and high strain-rate conditions representative of the ISBM process. This limitation is also highlighted by Billon [23].

In parallel, the modeling of biaxial stretch blow-molding has been the focus of extensive macroscopic investigations. As early as 1996, Schmidt et al. [24] introduced the concept of a deformation-dependent viscosity to describe the strain-hardening behavior observed during stretching. This approach was later adopted and refined by Cosson et al. [25] within a viscoplastic framework for PET, and subsequently extended to a large-strain visco-hyperelastic formulation by Chevalier et al. [26] and Luo et al. [27–29]. These developments progressively incorporated anisotropy and thermo-mechanical coupling to capture the self-heating phenomenon, often reaching 10–20 °C, and its strong influence on the material response during stretching. Building upon Buckley' glass-rubber viscoelastic model [30], several groups have proposed advanced numerical implementations. In particular, Pham et al. [31] and Mir et al. [32] developed elasto-visco-plastic constitutive

* Corresponding author.
E-mail address: luc.chevalier@univ-eiffel.fr (L. Chevalier).

https://doi.org/10.1016/j.polymertesting.2026.109120
Received 18 November 2025; Received in revised form 12 February 2026; Accepted 19 February 2026
Available online 20 February 2026

models coupled with thermo-mechanical effects and PV-T relationships to simulate the stretch blow-molding of PET preforms with improved accuracy. Similarly, Marckmann et al. [33] introduced a finite-element explicit formulation based on a dynamic visco-hyperelastic approach, later adopted in many industrial simulations. More recently, the Belfast group led by Menary and collaborators [34] implemented these constitutive equations within Abaqus, combining strain-rate- and temperature-dependent behavior with experimental validation through free-stretch-blow trials [35]. Their most recent developments introduce the neural networks to "learn" material behavior from extensive free-blow experiments, as reported by Teng et al. [36]. However, despite their substantial computational cost, these simulations can reproduce realistic thickness distributions but fail to predict the induced mechanical properties, except for a few fully interpolated models lacking physical grounding, such as those described in Ref. [2] and more recently in Ref. [28].

Recent constitutive models for semi-crystalline thermoplastics relies on thermo-mechanically coupled finite-strain formulations, often incorporating temperature-dependent material parameters and, in some cases, evolving crystallinity [37,38]. These approaches primarily aim at macroscopic response prediction under coupled thermal and mechanical loading. In parallel, multiphase descriptions have been proposed to represent distinct crystalline, amorphous, and interphase deformation mechanisms [39]. While physically detailed, these formulations typically introduce multiple internal variables that are not directly identified from in-situ experimental observations. More recently, finite-strain viscoelastic–viscoplastic frameworks have been proposed for thermoplastic polymers to capture time-dependent and irreversible deformation mechanisms [40,41]. These models are generally phenomenological and do not explicitly link mechanical response to the evolution of crystalline morphology during deformation.

Against this backdrop, the present work adopts a fundamentally different perspective. Rather than introducing additional phenomenological internal variables or fully thermo-coupled constitutive laws, the proposed framework is explicitly microstructure-driven and directly informed by in situ synchrotron SAXS measurements performed during equi-biaxial stretching of PET under conditions representative of the ISBM process. The constitutive description is based on a two-step mechanical homogenization strategy that combines the viscoelastic response of the amorphous phase with the quasi-elastic behavior of the crystalline phase. The size, morphology, orientation, and degree of crystallinity of the crystalline domains are experimentally quantified during deformation and directly incorporated into the model.

Thanks to the biaxial testing device developed at the MSME laboratory (see Ref. [42]) and the experiments conducted at the synchrotron, the authors recently established a model of the final microstructure which, through a two-step mechanical homogenization, enables accurate estimation of the final elastic properties [43,44]. These properties are measured on the tested specimens using digital image correlation (DIC), a technique that has proved effective in many applications [45–49]. Moreover, since the measurements are performed during stretching, the evolution of the microstructure can be better understood through the analysis of successive images.

In the present work, the term micro is used to refer to variables related to materials physics, such as the degree of crystallinity, crystalline lamella thickness, and macromolecular orientation, whereas macro refers to mechanical variables: stress, strain, and strain rate. Moreover, the modeling scale of the microstructure adopted in this study corresponds to a mesoscopic scale associated with the arrangement of crystalline lamellae (≈100 Å), which lies between the molecular scale (≈1 Å) and the specimen scale (≈1 mm = 10^7 Å). Building upon this analysis, the present study proposes a multiscale approach model that not only considers the conventional macroscopic variables (macro scale) such as stress and strain, but also incorporates the evolution of microstructural parameters (micro scale). Consequently, the simulation provides access to the predicted final microstructure, which can then be used to estimate the induced mechanical properties.

Despite the large separation between the lamellar scale and the specimen scale, this scale gap is sufficient to justify the analytical homogenization approach described in the following. This approach demonstrates that the nonlinear mechanical response, often introduced through explicitly nonlinear constitutive functions, naturally emerges here from the evolution of the material morphology, while preserving a formally "linear" formulation at each incremental step, i.e., with material parameters treated as constants rather than as state-dependent functions.

The paper is structured as follows:

- The "Materials and Methods" section presents the PET used in this study, the optimized geometry of the biaxial tensile specimens, the biaxial testing bench positioned on the SWING beamline of the synchrotron. The strain rate and temperature conditions for the tensile and relaxation tests, together with the characteristics of the SAXS measurements are also detailed.
- The "Theory" section summarizes the results of the two-step homogenization approach in the elastic case (DHA, "*double homogénéisation analytique*" in french) and justifies the simplifications made for its adaptation to the viscoelastic case, which is then developed and applied to the specific case of the equi-biaxial (EB) test.
- Finally, the "Results and Discussion" section presents the mechanical response measured during the EB test along with the corresponding SAXS patterns at different strain levels. The results are analyzed in relation to the final crystallinity ratio determined by DSC. The incremental scheme developed to iteratively simulate the material behavior by sequentially updating the evolving microstructure and the viscoelastic properties of the material is discussed.

2. Material and method

2.1. Material: PET sheets and biaxial specimen

The PET used in this study was provided by Polisan Hellas. Differential scanning measurements gave a melting temperature of 240-250 °C. The recommended molding temperature is in the range 270-290 °C. The average molecular weight M_n is 15000 g/mol. The PET square plates (125mmx125mm) with a thickness of 4 mm were injected at the PIMM laboratory. The tensile and density specimens were cut from the plates using a ProtoMAX water jet-cutting machine. These specimens are then machined in order to reduce the thickness of the region of interest, as shown on the CAD illustration of the optimized geometry (Fig. 1a).

The design criteria of the PET specimen used for biaxial stretching, including its geometry, thickness distribution, and optimization for ISBM-representative deformation paths, are detailed in Ref. [42]. As described in Ref. [42], the specimen geometry is specifically designed to localize deformation within the central region, where both the strain and the associated microstructural evolution are concentrated in this central area. The objective of the measurements is therefore not to obtain a spatial average over the entire specimen, but rather to capture the local evolution of the microstructure under controlled thermo-mechanical conditions. Consequently, the microstructural changes measured in this central region can be correlated with the local strain history and directly used to inform the proposed microstructure-driven modeling framework.

2.2. Biaxial elongation under synchrotron

The biaxial testing machine was designed, assembled, and tested at the MSME laboratory around 2020 (Fig. 1b). Its primary objective was to perform biaxial stretching tests with large strains, high strain rates, and regulated temperatures. Additionally, the machine was designed to be

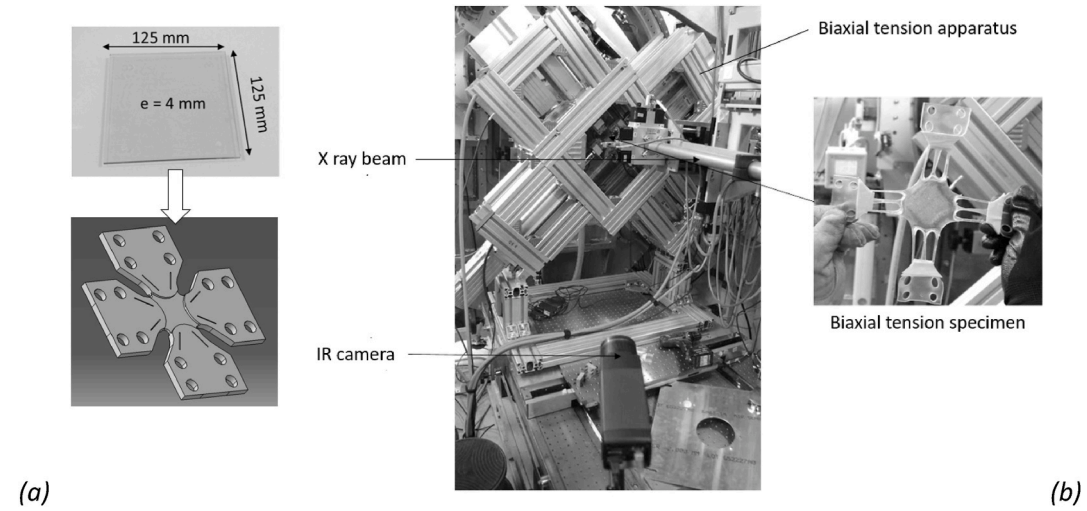

Fig. 1. (a) Injected PET plates and CAD of the optimized specimen; (b) biaxial elongation machine and biaxially stretched specimen.

compact and portable, allowing it to be used in various environments, including in-situ biaxial experiments under X-ray. The machine has a height of 1.2m and a width of 1.0m, weighing approximately 200 kg. It features four drives (CMMP-AS-C5-11A-P3-M0) controlling four motors (EMMS-AS 100-M-HS-RMB), each connected to an electric actuator (ESBF-BS-63-100-10P) from FESTO. These actuators allow independent tension or compression at speeds of up to 530 mm/s, with a maximum elongation of 200 mm via two face-to-face actuators, making the system suitable for tests similar to the stretch blow molding process. The cruciform specimen is mounted to the four independent Festo actuators, which are controlled by LabVIEW software using the Modbus TCP/IP protocol. This software not only manages the actuators but also acquires data from the force sensors installed between the actuators and the specimen grips. Heating is achieved through convection using a 3400 W heat gun with a maximum air flow of 800 l/min at 300 °C. A deflector ensures uniform temperature distribution across the specimen without direct exposure to the heat source. An IR camera (FLIR B250) measures the temperature distribution during the process. Additionally, a high-speed camera is used to capture images for Digital Image Correlation (DIC) analysis.

2.3. SAXS measures

SAXS measurements are carried out on the SWING beamline at Synchrotron SOLEIL. The wavelength λ is 1 Å and the measurement domain is limited to the angle defined by h/D, where $h = 80$ mm is the half-height of the receptor and $D = 3300$ mm is the distance between the specimen and the receptor, as illustrated on Fig. 2. This leads to a small angle range of 2θ equal to 0.024 rad or 1.4°. Following the classical definition, the magnitude q of the scattering vector is given by:

$$q = \frac{2\pi}{\lambda}\sin(\theta) \tag{1}$$

we obtain 2D patterns on a picture, where q varies from -0.15 Å^{-1} to 0.15 Å^{-1} in both directions. It should be noted that the specimens are placed in the biaxial apparatus at an angle of 45° relative to the horizontal direction.

3. Theory

We propose here to use the Laplace–Carson transform in order to adapt the analytical double homogenization scheme developed for an elastic model to the viscoelastic case, which corresponds to the behavior of polymers above their glass transition temperature. The principle of this equivalence is detailed in the appendix, and it allows us to apply to the relaxation function tensors $[C_a(t)]$ and $[C_c(t)]$, corresponding respectively to the amorphous and crystalline phases, the same formulas as those developed for the elastic homogenization problem. Before doing so, we will examine these relations for the sake of simplification.

As detailed in Refs. [43,44] and recalled in appendix A, we have proposed a framework, illustrated on Fig. 3. It can be shown that most of formulae are identical to mixture rules for parallel or series structure. Thes simplification will be used in our viscoelastic homogenization.

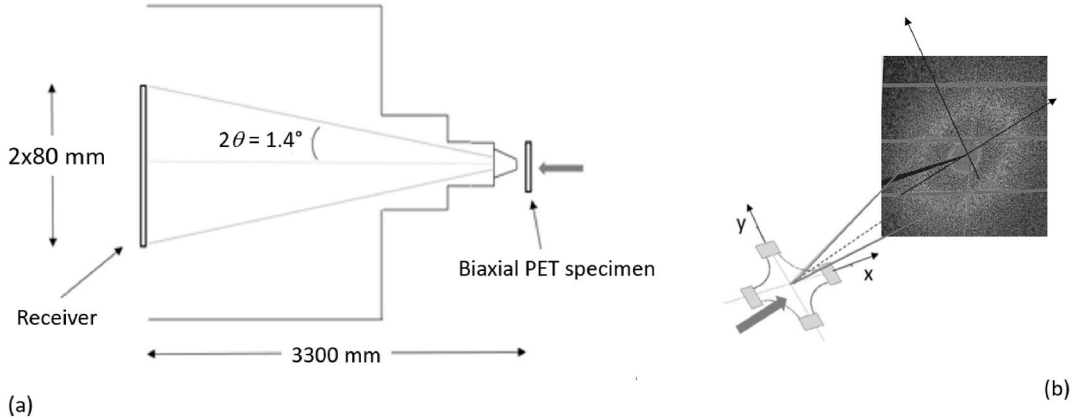

Fig. 2. (a) Geometrical characteristics; (b) SAXS figure and specimen principal axis disposed at ±45°.

3.1. Tensor of relaxation functions

Thanks to the Laplace-Carson transform, the viscoelastic behavior of each phase may be written in the following way:

$$\underline{\widehat{\sigma}}(p) = [\widehat{C}^{a}(p)]\underline{\widehat{\varepsilon}}(p) \text{ and } \underline{\widehat{\sigma}}(p) = [\widehat{C}^{c}(p)]\underline{\widehat{\varepsilon}}(p) \quad (2)$$

where $\underline{\widehat{\sigma}}(p)$ and $\underline{\widehat{\varepsilon}}(p)$ are respectively the transformed stress and strain tensors in each phase. $[\widehat{C}^{a}(p)]$ and $[\widehat{C}^{c}(p)]$ are the transformed relaxation function tensors of the amorphous and crystal phases. We assume the first is isotropic while the last is transversally isotropic around the 2-axis. We also choose a unique relaxation times θ_a and θ_c respectively of the amorphous and crystal phases. Thus, each relaxation function in the natural space writes:

$$C_{ij}^{a}(t) = C_{ij}^{a}\exp(-t/\theta_a) \text{ and } C_{ij}^{c}(t) = C_{ij}^{c}\exp(-t/\theta_c) \quad (3)$$

And transforms as follow:

$$\widehat{C}_{ij}^{a}(p) = \frac{\theta_a C_{ij}^{a} p}{1+\theta_a p} \text{ and } \widehat{C}_{ij}^{c}(p) = \frac{\theta_c C_{ij}^{c} p}{1+\theta_c p} \quad (4)$$

Considering the previous section, three cases are to be studied. The first concerns the components C_{11}, C_{33}, C_{13} and C_{55} and is straightforward thanks to the linearity of the Laplace-Carson transform. These terms write:

$$C_{ij}^{bi}(t) = \alpha_a C_{ij}^{a}\exp\left(-\frac{t}{\theta_a}\right) + \alpha_c C_{ij}^{c}\exp\left(-\frac{t}{\theta_c}\right) \quad (5)$$

with $\alpha_a = 1\text{-}\alpha_c$. The homogenized component appears to be a two-mode Prony series. The components C_{22}, C_{44} and C_{66} can also be treated easily

$$\widehat{C}_{ij}^{bi}(p) = \frac{1}{\frac{\alpha_a}{\widehat{C}_{ij}^{a}(p)} + \frac{\alpha_c}{\widehat{C}_{ij}^{c}(p)}} = \frac{C_{ij}^{a}C_{ij}^{c}}{\alpha_a C_{ij}^{c} + \alpha_c C_{ij}^{a}} \times \frac{p}{p + \frac{\alpha_a C_{ij}^{c}\theta_c + \alpha_c C_{ij}^{a}\theta_a}{\theta_a\theta_c\left(\alpha_a C_{ij}^{c} + \alpha_c C_{ij}^{a}\right)}} \quad (6)$$

Thus, the inverse Laplace-Carson transform leads to a decreasing exponential function:

$$C_{ij}^{bi}(t) = C_{ij}^{eq}\exp\left(-\frac{t}{\theta_{eq}}\right) \Rightarrow \begin{cases} C_{ij}^{eq} = \dfrac{1}{\frac{\alpha_a}{\widetilde{C}_{ij}^{a}} + \frac{\alpha_c}{\widetilde{C}_{ij}^{c}}} \\ \theta_{eq} = \dfrac{\frac{\alpha_a}{\widetilde{C}_{ij}^{a}} + \frac{\alpha_c}{\widetilde{C}_{ij}^{c}}}{\frac{\alpha_a}{\theta_a\widetilde{C}_{ij}^{a}} + \frac{\alpha_c}{\theta_c\widetilde{C}_{ij}^{c}}} \end{cases} \quad (7)$$

Finally, thanks to the simplification of the numerator of the expression of Eq. (8), the last terms C_{12} and C_{23} also lead to a decreasing exponential function that is proportional to the C_{22} component:

$$\widehat{C}_{12}^{bi}(p) = \widehat{C}_{23}^{bi}(p) = \frac{\alpha_c\frac{\widehat{C}_{12}^{c}(p)}{\widehat{C}_{22}^{c}(p)} + \alpha_a\frac{\widehat{C}_{12}^{a}(p)}{\widehat{C}_{22}^{a}(p)}}{\frac{\alpha_c}{\widehat{C}_{22}^{c}(p)} + \frac{\alpha_a}{\widehat{C}_{22}^{a}(p)}} = \left(\alpha_c\frac{C_{12}^{c}}{C_{22}^{c}} + \alpha_a\frac{C_{12}^{a}}{C_{22}^{a}}\right) \times \widehat{C}_{22}^{bi}(p)$$

$$\Rightarrow C_{12}^{bi}(t) = C_{23}^{bi}(t) = \left(\alpha_c\frac{C_{12}^{c}}{C_{22}^{c}} + \alpha_a\frac{C_{12}^{a}}{C_{22}^{a}}\right)C_{22}^{bi}(t) \quad (8)$$

After this first homogenization step, six relaxation moduli must be determined from the amorphous and crystal behavior. Among them, three ($C_{11}^{bi} = C_{33}^{bi}$, C_{13}^{bi}, and C_{55}^{bi}) involve the two relaxation times θ_a and θ_c. In contrast, the remaining three ($C_{12}^{bi} = C_{23}^{bi}$, C_{22}^{bi}, and $C_{44}^{bi} = C_{66}^{bi}$) involve only a single relaxation time each, which is neither that of the amorphous phase nor that of the crystalline phase. It is worth noting that the relaxation time of C_{12}^{bi} or C_{23}^{bi} is identical to that of C_{22}^{bi}.

The rotation step leads to linear formulae and are not transformed by the Laplace-Carson transform:

$$\begin{aligned}
C_{11}(\varphi) &= C_{11}^{bi}\cos^4\varphi + C_{22}^{bi}\sin^4\varphi + \left(2C_{12}^{bi} + 4C_{66}^{bi}\right)\cos^2\varphi\sin^2\varphi \\
C_{22}(\varphi) &= C_{11}^{bi}\sin^4\varphi + C_{22}^{bi}\cos^4\varphi + \left(2C_{12}^{bi} + 4C_{66}^{bi}\right)\cos^2\varphi\sin^2\varphi \\
C_{33}(\varphi) &= C_{33}^{bi} \\
C_{44}(\varphi) &= C_{55}^{bi}\sin^2\varphi + C_{44}^{bi}\cos^2\varphi \\
C_{55}(\varphi) &= C_{55}^{bi}\cos^2\varphi + C_{44}^{bi}\sin^2\varphi \\
C_{66}(\varphi) &= \left(C_{11}^{bi} + C_{22}^{bi} - 2C_{12}^{bi}\right)\cos^2\varphi\sin^2\varphi + C_{66}^{bi}\left(\cos^2\varphi - \sin^2\varphi\right)^2 \\
C_{12}(\varphi) &= \left(C_{11}^{bi} + C_{22}^{bi} - 4C_{66}^{bi}\right)\cos^2\varphi\sin^2\varphi + C_{12}^{bi}\left(\cos^4\varphi + \sin^4\varphi\right) \\
C_{13}(\varphi) &= C_{13}^{bi}\cos^2\varphi + C_{23}^{bi}\sin^2\varphi \\
C_{23}(\varphi) &= C_{23}^{bi}\cos^2\varphi + C_{13}^{bi}\sin^2\varphi \\
C_{16}(\varphi) &= \left(C_{11}^{bi} - C_{12}^{bi} - 2C_{66}^{bi}\right)\cos^3\varphi\sin\varphi + \left(C_{12}^{bi} - C_{22}^{bi} + 2C_{66}^{bi}\right)\cos\varphi\sin^3\varphi \\
C_{26}(\varphi) &= \left(C_{12}^{bi} - C_{22}^{bi} + 2C_{66}^{bi}\right)\cos^3\varphi\sin\varphi + \left(C_{11}^{bi} - C_{12}^{bi} - 2C_{66}^{bi}\right)\cos\varphi\sin^3\varphi
\end{aligned} \quad (9)$$

The second step of homogenization will be presented in the next section, for the particular case of equi-biaxial elongation.

3.2. Application to EB case

In the equi-biaxial case, at each time step, the only non-zero stress increments are $d\sigma_{xx}$ and $d\sigma_{yy}$, both denoted $d\sigma$; all other components vanish. On the strain side, the in-plane strain increments are $d\varepsilon_{xx}$ and $d\varepsilon_{yy}$, denoted $d\varepsilon$. According to the incompressibility condition, $d\varepsilon_{zz} = -$

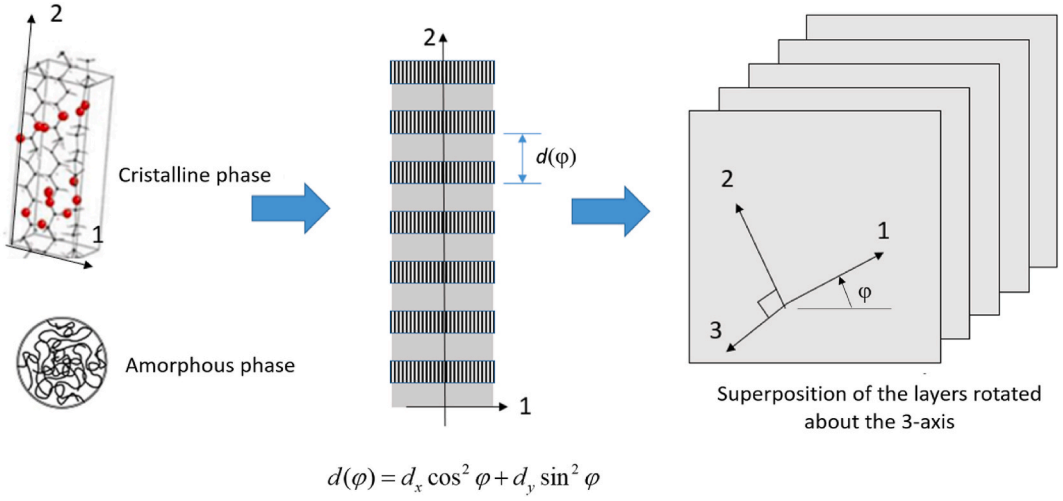

$$d(\varphi) = d_x \cos^2\varphi + d_y \sin^2\varphi$$

Fig. 3. Two steps homogenization framework.

$2\,d\varepsilon$, and there is no angular distortion. For the incompressible case, the stresses are defined by:

$$\underline{\sigma} = \underline{\Sigma} - pI \tag{10}$$

where $\underline{\Sigma}$ is the deviatoric stress tensor and p the hydrostatic pressure associated with the incompressibility condition. This implies:

$$d\sigma = d\Sigma - d\Sigma_{zz} \tag{11}$$

In the Laplace–Carson space, the two extra stresses are linearly related to the strain increment by:

$$\left.\begin{aligned} d\widehat{\Sigma} &= (\widehat{C}_{11}^{\ PET} + \widehat{C}_{12}^{\ PET} - 2\widehat{C}_{13}^{\ PET})\,d\widehat{\varepsilon} \\ d\widehat{\Sigma}_{zz} &= (\widehat{C}_{13}^{\ PET} + \widehat{C}_{23}^{\ PET} - 2\widehat{C}_{33}^{\ PET})\,d\widehat{\varepsilon} \end{aligned}\right\} \Rightarrow d\widehat{\sigma} = (\widehat{C}_{11}^{\ PET} + \widehat{C}_{12}^{\ PET} - 4\widehat{C}_{13}^{\ PET} + 2\widehat{C}_{33}^{\ PET})\,d\widehat{\varepsilon} \tag{12}$$

Hence, it is not necessary to develop all the terms of the homogenized tensor $[C^{PET}]$, but only the four components appearing in Eq. (12). Recall that, for a stack of N identical layers rotated by an angle $2\pi/N$, the relations obtained for the second homogenization step are:

$$\widehat{C}_{11}^{\ PET} = \frac{1}{N}\sum_{i=1}^{N} \widehat{C}_{11}^{\ \varphi i},\ \widehat{C}_{12}^{\ PET} = \frac{1}{N}\sum_{i=1}^{N} \widehat{C}_{12}^{\ \varphi i},\ \widehat{C}_{13}^{\ PET} = \frac{\sum_{i=1}^{N} \frac{\widehat{C}_{13}^{\ \varphi i}}{\widehat{C}_{33}^{\ \varphi i}}}{\sum_{i=1}^{N} \frac{1}{\widehat{C}_{33}^{\ \varphi i}}},\ \widehat{C}_{33}^{\ PET} = \frac{1}{\frac{1}{N}\sum_{i=1}^{N} \frac{1}{\widehat{C}_{33}^{\ \varphi i}}} \tag{13}$$

Since the components no longer depend on the rotation angle φ_i, these relations simplify and can be written in the natural coordinate system as:

$$\begin{aligned} C_{11}^{\ PET}(t) &= 0.375\left(C_{11}^{\ bi}(t) + C_{22}^{\ bi}(t)\right) + 0.125\left(2C_{12}^{\ bi}(t) + 4C_{66}^{\ bi}(t)\right) \\ C_{12}^{\ PET} &= 0.125\left(C_{11}^{\ bi}(t) + C_{22}^{\ bi}(t) - 4C_{66}^{\ bi}(t)\right) + 0.75C_{12}^{\ bi}(t) \\ C_{13}^{\ PET} &= 0.5\left(C_{13}^{\ bi}(t) + C_{23}^{\ bi}(t)\right) \\ C_{33}^{\ PET}(t) &= C_{33}^{\ bi}(t) \end{aligned} \tag{14}$$

The numerical coefficients result from the averaging of sine and cosine products raised to various powers in Eq. (9). The expressions of the components $C_{ij}^{bi}(t)$ are given by Eqs. (5)–(8); all are decreasing exponential functions. Thus, the relationship between $d\sigma$ and $d\varepsilon$ in the natural coordinate system can be interpreted as a Prony series consisting of four spring–dashpot associations in parallel, each corresponding to one relaxation time:

$$\theta_I = \theta_a, \theta_{II} = \theta_c, \theta_{III} = \theta_{22}^{eq}, \theta_{IV} = \theta_{66}^{eq} \tag{15}$$

The associated moduli are obtained by grouping all terms that share the same relaxation time, recalling that $C_{11}^{bi} = C_{33}^{bi}$ and $C_{12}^{bi} = C_{23}^{bi}$:

$$\begin{aligned} C^{PET}(t) &= C_{11}^{\ PET}(t) + C_{12}^{\ PET}(t) - 4C_{13}^{\ PET}(t) + 2C_{33}^{\ PET}(t) \\ &= 2.5C_{11}^{\ bi}(t) + 0.5C_{22}^{\ bi}(t) - C_{12}^{\ bi}(t) - 2C_{13}^{\ bi}(t) \end{aligned} \tag{16}$$

where it can be seen that the term C_{66}^{bi} vanishes, thus reducing the series to three terms (Fig. 4), with the corresponding modulus given by:

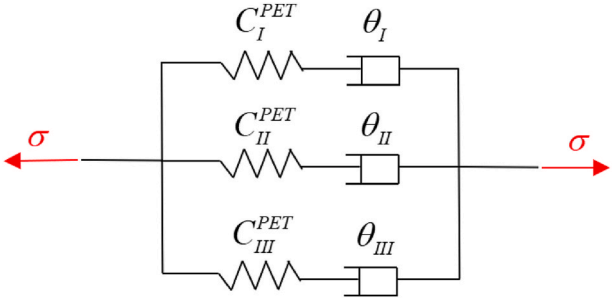

Fig. 4. Illustration PET behavior during equi-biaxial elongation modelled by a Prony series with 3 branches.

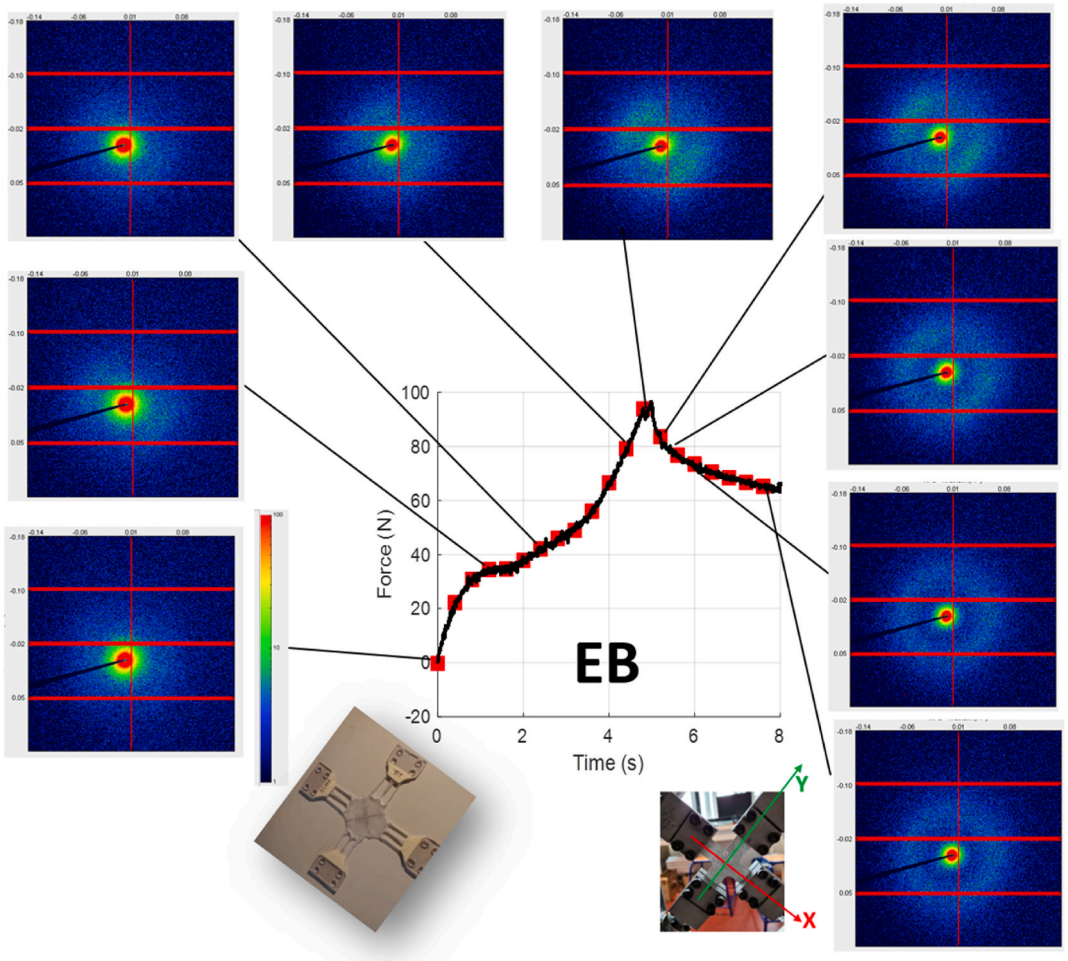

Fig. 5. Equi-biaxial elongation and relaxation of the PET specimen under X-ray beam.

$$
\begin{aligned}
C_I^{PET} &= (1-\alpha_c)(2.5{C_{11}}^a - 2{C_{13}}^a)\\
C_{II}^{PET} &= \alpha_c(2.5{C_{11}}^c - 2{C_{13}}^c)\\
C_{III}^{PET} &= \left(0.5 - \alpha_c\frac{{C_{12}}^c}{{C_{22}}^c} - (1-\alpha_c)\frac{{C_{12}}^a}{{C_{22}}^a}\right){C_{22}}^{eq}
\end{aligned}
\tag{17}
$$

3.3. Coupling between microstructure and stress

To complete the description of how the microstructure influences the material behavior, it is also necessary to describe how the stress generated during deformation affects the microstructure itself. To this end, we use a modeling approach derived from the Avrami model [50–52], originally developed for isothermal crystallization and later extended by Nakamura et al. [53]. Other authors, including Hieber [54] and Pople et al. [55], proposed incremental forms of this model in order to successfully simulate crystallization during temperature variations:

$$
\frac{d\chi}{dt} = nk^{1/n}(1-\chi)(-\ln(1-\chi))^{n-1} \tag{18}
$$

where χ is the reduced crystallinity ratio, defined as the ratio between the degree of crystallinity at time t and the maximum possible crystallinity for the material considered.

This differential form has already been used in several studies on PET, notably in Refs. [56–58] by some of the present authors, in the context of thermal crystallization.

When mechanical effects drive both molecular orientation and crystallization, the Avrami factor k can be made to depend not only on temperature but also on the strain ε or strain-rate $\dot{\varepsilon}$ or more globally, on the applied stress σ: the higher are theses variables, the stronger its driving effect on crystallization.

We therefore seek a simple stress-dependent relationship $k(\varepsilon, \dot{\varepsilon}, \sigma)$ capable of accurately representing our experimental results: both the material behavior and the evolution of the microstructure.

4. Results and discussion

4.1. Biaxial tensile test results

Fig. 5 summarizes the results obtained from the equi-biaxial tensile tests conducted using the biaxial machine under the synchrotron beam Swing at Soleil. The test was performed at 95 °C, with a tensile speed of 10 mm/s applied to each grip. DIC measures show that the 100 mm elongation is heterogeneous and leads to a maximum nominal strain of 1.7 in the center of the specimen. The mean strain rate is then equal to 0.34 s^{-1} and is relatively low compared to the stretch blow molding process. This limitation is related to the current configuration of the biaxial testing device, which was initially optimized for in-situ synchrotron measurements rather than for achieving extreme deformation levels and strain rates simultaneously. Nevertheless, it is sufficient to clearly observe the typical strain-hardening effect of stretched PET and to capture enough SAXS images to follow the morphology evolution. The biaxial stretching apparatus is currently being upgraded, and several design improvements are under development to enable both larger attainable strains (>3) and higher strain rates (>5s^{-1}). These developments will be the subject of future work and are expected to extend the experimental window of the present approach.

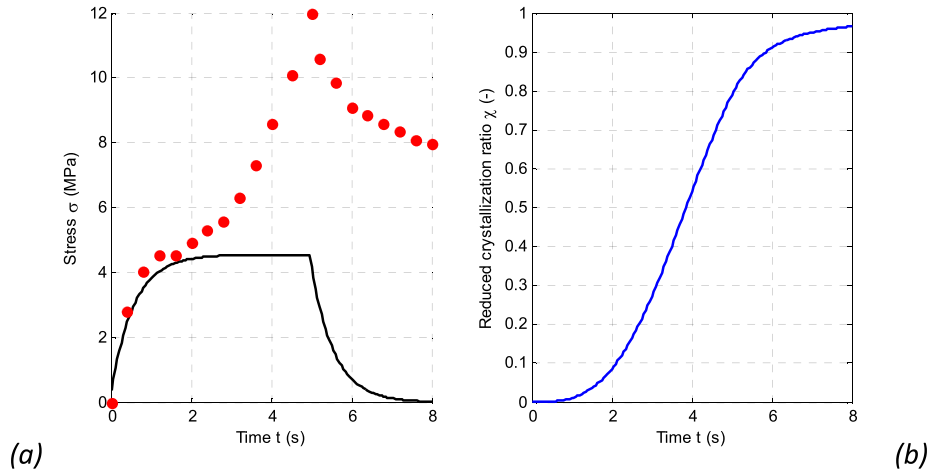

Fig. 6. Equi-biaxial elongation and relaxation of the PET specimen. (a) spots are experimental data, the curve is a simple Maxwell modeling without incremental adaptation of the morphology; (b) evolution of the reduced crystallinity ratio based on the simple linear dependence with the stress (see section 4.2).

One can see that a periodic crystallization of the material begins at approximately 4 s (80 mm of elongation), coinciding with the middle of the strain-hardening regime. This regime is strongly related to the reinforcement of the material due to the orientation and/or crystallization of the polymer. A non-uniform change in morphology can be observed, as evidenced by the intensity of the circular SAXS halo, which is higher in the X direction. At 5 s, the elongation stops, and the relaxation phase begins: the stress reduces while the intensity of the circular halo stabilizes. From 6 s to the end, the SAXS pattern does not change: the uniform circular shape remains, indicating an isotropic distribution of the morphology in the X,Y plane.

This morphology is composed of a regular crystalline lamellae distribution linked by an oriented amorphous phase. One can observe that the intensity of the halo, higher in the X direction than in the Y one at the end of the elongation, gradually becomes more uniform. This uniformity is likely the result of the rotation of the crystalline lamellae around the Z-direction, still possible while the temperature is high enough and driven by unbalanced thermodynamic forces. This mobility can be justified in light of the works by Refs. [12–16], and more recently [17], which show that crystallization develops both during stretching and during relaxation. Chain mobility is therefore sufficient even at temperatures relatively close to T_g. It should also be noted that several studies [27,29] report a temperature increase of about ten degrees or more during stretching due to viscous dissipation, which leads to self-heating. The other possible explanation for the decrease in SAXS intensity would be that stretching along the X direction "breaks" part of the periodicity along Y, which appears physically unlikely.

The maximum of the intensity peaks appearing between 4.2 and 4.8 s is positioned at $q_x = 0.07$ Å^{-1}, indicating the interlamellar spacing is equal to $d_x \approx 90$ Å. DSC measures performed on the final specimen indicate the ultimate crystallinity ratio of 42%. We restricted our analysis to the determination of the long period d of the periodic distribution of crystalline lamellae. In principle, the thickness l_c of the crystalline lamellae can be determined from SAXS data by analyzing the slope discontinuities of the correlation function $\gamma(z)$. Consequently, the determination of the amorphous layer thickness l_a and of the volume crystallinity α_c is straightforward. However, this approach is highly sensitive to noise and did not yield results that were consistent with our experimental data. Another method was also considered, the lamellar stack fit approach; however, the results obtained were again not conclusive. Specifically, fitting performed with a fixed long period d yields crystalline lamellar thicknesses l_c that decrease during stretching, whereas a monotonic increase in the degree of crystallinity would be expected.

From the force-displacement curve, it is possible to provide the stress-time curve plotted on Fig. 6a, where the initial part highlight a classical Maxwell behavior that evolves with a strain hardening effect, characteristic of the PET behavior in elongation. After 5 s, the stress decreases during the relaxation step but does not appear to decrease to zero.

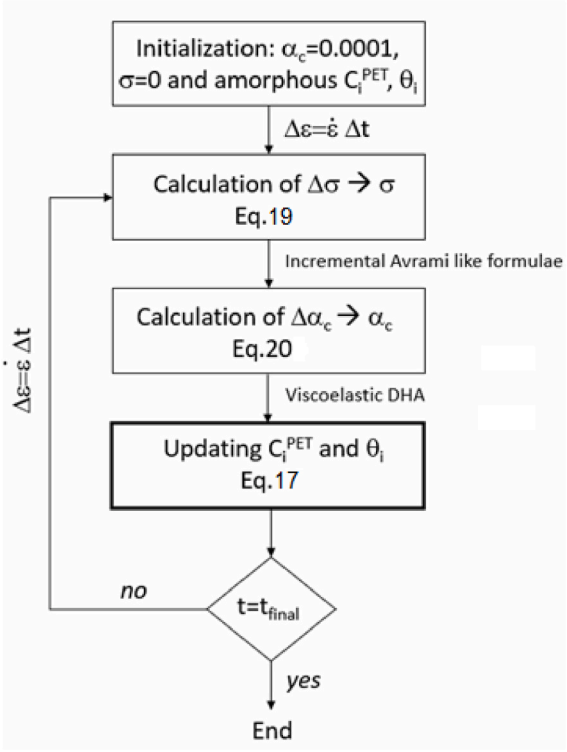

Fig. 7. Incremental simulation of the equi-biaxial elongation test.

4.2. Incremental modeling of the EB test

The rotation of the lamellae and the correction of the initial in-plane anisotropy arise from two main effects: (i) specimen imperfections, which allow deformation to develop preferentially along the Y direction before the X direction, and (ii) structural hardening, which progressively rebalances the deformation between the two directions. The evolution of the lamellar periodicity, in contrast, is likely associated with a certain

elastic response of the stretched amorphous phase. In the first case, this deformation imbalance cannot be explicitly modelled. In the second case, the effect was neglected in the present work as a first approximation, but it remains an important aspect for future investigation.

In practice, at a given instant t_n where the stress $\sigma(t_n)$ is known, the stress increment $\Delta\sigma$ can be calculated by summing the three partial increments $\Delta\sigma_I + \Delta\sigma_{II} + \Delta\sigma_{III}$, each obtained by solving the Maxwell law in its differential form:

$$\sigma_i + \theta_i\dot{\sigma}_i = \theta_i C_i^{PET}\dot{\varepsilon} \Rightarrow \Delta\sigma_i = \left(C_i^{PET}\dot{\varepsilon}(t_n) - \frac{\sigma_i(t_n)}{\theta_i}\right)\Delta t \text{ for } i = I, II, III \quad (19)$$

By summing these three contributions, the stress $\sigma(t_{n+1})$ can be evaluated. Next, the crystallinity ratio is updated considering the incremental form of Eq. (18):

$$\dot{\chi} = nk^{1/n}(1-\chi)(-\ln(1-\chi))^{n-1} \Rightarrow \Delta\chi = nk(\sigma)^{1/n}(1-\chi)(-\ln(1-\chi))^{n-1}\Delta t \quad (20)$$

Then, the analytical viscoelastic double-step homogenization (DHA-VE) is applied to update the moduli and relaxation times. This step is the most important in the iterative process described in Fig. 7 (highlighted box), as it will lead to the observed strain hardening effect. At this stage, two questions remain to be addressed:

1. How should the initial relaxation times of the two phases, as well as the initial moduli C_{11}, C_{22}, C_{12} and C_{13} of the amorphous and crystalline phases, be selected?
2. What functional form should be chosen for the Avrami factor $k(\varepsilon, \dot{\varepsilon}, \sigma)$ as a function of stress?

For the equi-biaxial test carried out under synchrotron radiation, an average strain rate of 0.34 s^{-1} was applied, kept constant for 5 s, and then set to zero, while a total strain of 170 % was maintained for a few additional seconds. The crystallinity ratio was zero at the beginning of the test and evolved such that significant crystallization appeared after 3.6 s, reaching saturation around 6 s.

Thus, by choosing for example, a simple linear relationship for the Avrami factor, $k(\sigma) = a_\sigma.\sigma/\sigma_0$, where $\sigma_0 = 1$ MPa, one can use the experimental stress data (red points in Fig. 6a) to obtain the predicted curve (Fig. 6b) with $a_\sigma = 0.0027$ $s^{-3}MPa^{-1}$. This provides an answer to question 2, but others are possible as we will see in the discussion section.

Distinguishing between the respective contributions of the oriented amorphous phase and the crystalline phase to the reinforcement associated with the morphological changes of the material is a complex issue. The orientation of polymer chains in the amorphous phase is an important factor to consider at room temperature, whereas above T_g the chain mobility becomes sufficiently high for the assumption of isotropy to remain adequate to obtain reasonable orders of magnitude. Consequently, we consider an isotropic behavior for the amorphous phase.

Regarding the initial behavior of the amorphous phase, its elastic modulus E_a and relaxation time θ_a can easily be evaluated from the slope and curvature at the beginning of the stress–time curve (Fig. 6a), since the strain rate is constant. This yields to $E_a = 8.25$ MPa for $\upsilon_a = 0.4$ and $\theta_a = 0.90$ s.

The crystalline phase is stiffer than the amorphous phase and clearly anisotropic. It is therefore considered quasi-elastic (in practice, using a very large relaxation time is used, $\theta_c = 10^6$ s), with its moduli derived from the elastic stiffness tensor [C_c] at ambient temperature T_a, taken from the literature [59]. These moduli are scaled by a global temperature-dependent factor $f_c(T°)$, such that:

$$[C_c(T°)] = f_c(T°) \times [C_c(T_a)] \quad (21a)$$

With:

$$[C_c] = \begin{bmatrix} 7070 & 5070 & 5460 & 0 & 0 & 0 \\ 5070 & 118000 & 5070 & 0 & 0 & 0 \\ 5460 & 5070 & 7070 & 0 & 0 & 0 \\ 0 & 0 & 0 & 1620 & 0 & 0 \\ 0 & 0 & 0 & 0 & 1120 & 0 \\ 0 & 0 & 0 & 0 & 0 & 1620 \end{bmatrix} \text{ in MPa} \quad (21b)$$

This amounts to determining the scaling coefficient f_c at the test temperature. For f_c ($T = 95$ °C) = 0.0045, the resulting curve is shown in Fig. 8, where the following observations can be made:

(i) The tensile phase is well represented, both in terms of curvature and peak level;
(ii) The initial part of the relaxation phase exhibits a correct slope;
(iii) The stress does not return to zero, indicating a residual elastic component;
(iv) The overall relative deviation from the experimental data is only 0.13%, which is remarkably small.

4.3. Discussion on influence of temperature and strain rate

It is necessary to verify the consistency of the model with known experimental results beyond the EB test performed under synchrotron radiation. To this end, we use results obtained from a series of tests conducted in the MSME laboratory on the same biaxial testing device and using identical specimens [42]. The three temperatures and the

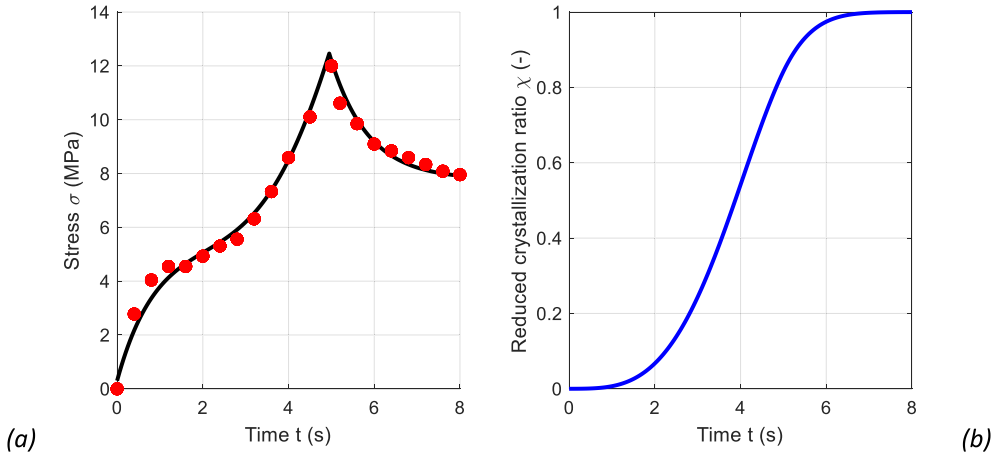

Fig. 8. Experimental data and identified DHA-VE model. (a) stress versus time model (continuous line) compared to experiment data (dot); (b) reduced crystallinity ratio versus time.

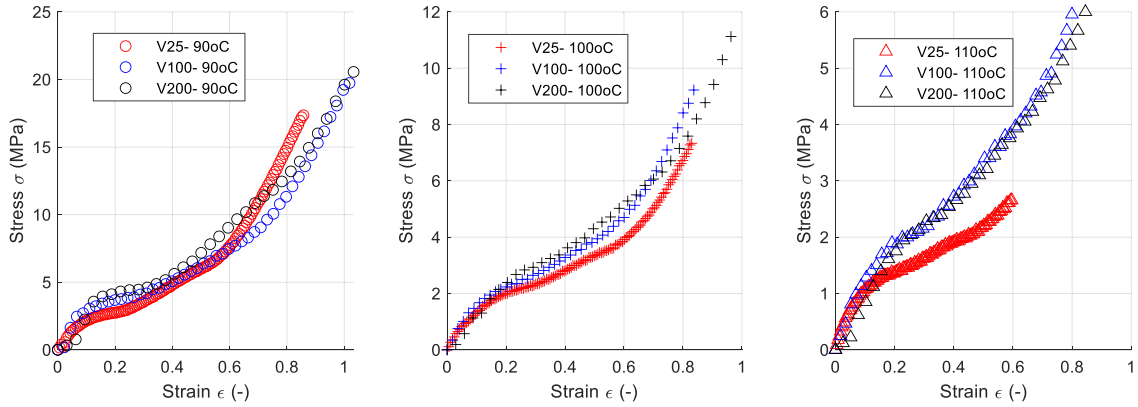

Fig. 9. Stress versus strain plots for equi-biaxial elongation tests at different temperature and velocity, experimental data from [42].

Table 1
Moduli and relaxation time identification from the beginning of stress-time curves.

T = 90 °C					
V (mm/s)	*$\dot{\varepsilon}$ (s^{-1})*	*Initial slope (MPa/s)*	*Inflexion stress (MPa)*	*θ_a (s)*	*E_a (MPa)*
25	0.47	23.1	2.75	0.12	24.55
100	2.25	100	3.75	0.04	22.22
200	4.68	150	4.5	0.03	16.03
			Mean values	0.06	20.93
T = 100 °C					
25	0.44	10	2.25	0.23	11.36
100	1.8	41.2	2.49	0.06	11.44
200	4.36	76.1	3.24	0.04	8.73
			Mean values	0.11	10.51
T = 110 °C					
25	0.32	6.25	1.5	0.24	9.77
100	1.73	22.7	2.09	0.09	6.57
200	3.82	34.2	2.34	0.07	4.48
			Mean values	0.13	6.94

three strain rates were chosen based on the values used in the biaxial stretch blow molding process. The preform, which is subsequently transformed into a bottle, is stretched above the glass transition temperature, typically within the temperature range of 90 to 110 °C. The strain rates generated during blow molding are high, on the order of 10 to 50 s^{-1}, and the process induces tensile strains of approximately 100 to 300% in both the longitudinal and circumferential directions of the bottle. The following tests conditions are supposed to reproduce these conditions as closely as possible. The series referred to in Fig. 9 was conducted earlier as part of a previous study. At that time, tests were performed at 90 and 100 °C, but unfortunately, not at 95 °C.

The following observations can be made:

1. The maximum stresses decrease progressively as the temperature increases;
2. All curves exhibit a strain-hardening effect as the deformation increases;
3. Except for the curve corresponding to $V = 25$ mm/s and $T = 110$ °C, the strain rate effect does not clearly appear on the stress–strain curves, which implies a weak and nonlinear contribution of the strain rate.

Table 2
Parameters of the DHA-VE model identified from EB tests at three different temperature, using the full set of three stretching velocities for each temperature.

T (°C)	E_a (MPa)	θ_a (s)	f_c	a_ε	b_ε
90	7.83	0.992	0.125	0.04	0.016
100	4.609	0.989	0.0402	0.04	0.016
110	3.315	1.407	0.0031	0.04	0.016

From the duration of the tests and the maximum strain, one can evaluate the mean strain rate, that varies from 0.3 to 4.7 s^{-1}. We can apply the same methodology as before: based on the stretching duration and the maximum strain, we determine the average strain rate during the test. Using the ratio between the stress at the inflection point of the curve and the initial slope, we can deduce the relaxation time and then calculate the amorphous modulus E_a from the slope and the strain rate. The resulting values are given in Table 1.

It can be seen that, for a given temperature, the modulus values vary, but the most significant variation concerns the relaxation time, which is much higher for the 25 mm/s strain rate than for the other two. Nevertheless, the averages calculated for each temperature remain within consistent orders of magnitude and will be used as initial estimates in the identification process. The modulus decreases with temperature, which is a classical tendency, whereas the relaxation time increases, indicating an increase in viscosity: this behavior is less classical.

Starting from these initial values, we perform a minimization of the discrepancy between the experimental data points and the results obtained from our incremental simulation. Several simple functional forms were tested to model the mechanical influence on the Avrami coefficient k. A linear dependence on stress, as proposed in Eq. (21), is the most straightforward assumption:

$$k(\sigma) = a_\sigma \left(\frac{\sigma}{\sigma_0}\right) \text{ with } \sigma_0 = 1MPa \tag{21}$$

The parameter a_σ may vary with temperature and must therefore be identified together with E_a, θ_a, and f_c for each set of curves. The difficulty of this modeling approach lies in the strong coupling between the parameters, since the stress depends both on the constitutive behavior and the microstructure evolution. Consequently, this formulation can easily lead to divergence.

A dependence on strain rate alone does not correctly capture crystallization, which continues during the relaxation phase, and a dependence on strain alone is inconsistent with the observed competition between test duration and crystallization kinetics. Therefore, we select a simple function involving two parameters, a_ε and b_ε, accounting for both strain and strain rate, to be identified:

$$k(\sigma) = a_\varepsilon \left(\frac{\dot{\varepsilon}}{\dot{\varepsilon}_0}\right) + b_\varepsilon \left(\frac{\varepsilon}{\varepsilon_0}\right) \text{ with } \dot{\varepsilon}_0 = 1s^{-1} \text{ and } \varepsilon_0 = 1 \tag{22}$$

To fit the different curves, we start from an initial estimate of the

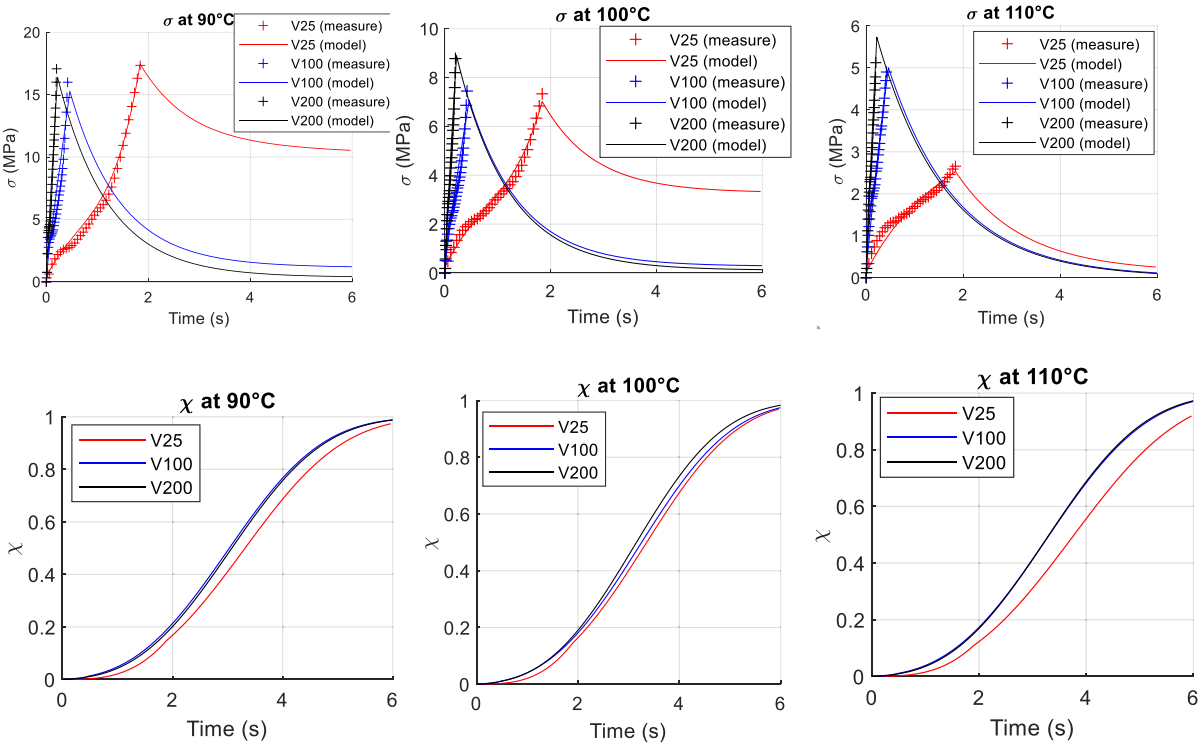

Fig. 10. Stress versus time plots for equi-biaxial elongation tests at different temperatures and velocities, as predicted by the DHA-VE model, together with the corresponding reduced crystallization ratio.

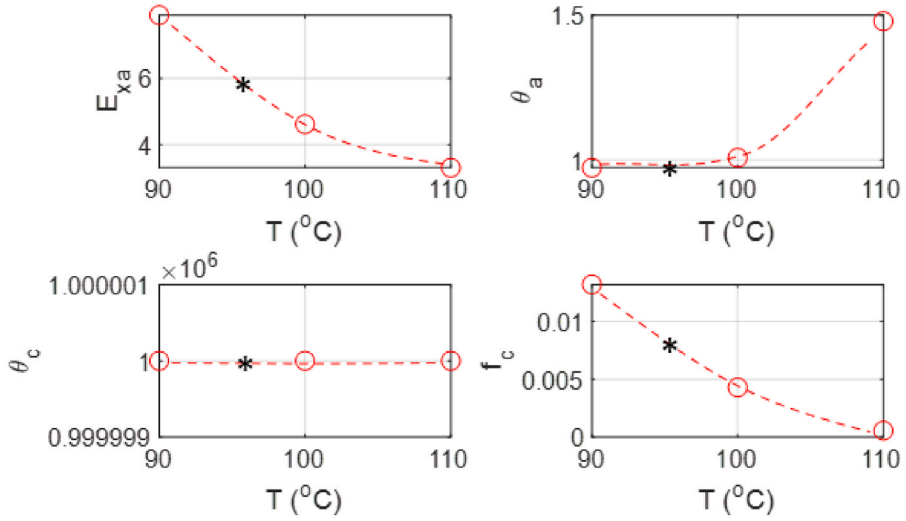

Fig. 11. Evolution of the DHA-VE model parameters versus temperature.

amorphous moduli and of the parameters $a_\varepsilon = 0.04\,s^{-1}$ and $b_\varepsilon = 0.016\,s^{-1}$, obtained from the 95°C synchrotron test curve, for which relaxation data are available. We then minimize the deviation by adjusting E_a, θ_a, and f_c for each temperature, using simultaneously the three stretching velocities at that temperature. The resulting parameter sets are summarized in Table 2.

The curves shown in Fig. 10 represent the stress evolution over time predicted by the DHA-VE model during the biaxial tensile tests performed at different temperatures and strain rates. Each tensile loading stage is followed by a relaxation phase extending up to 6 s.

It is interesting to note that the curves corresponding to the lowest strain rates do not fully relax to zero stress, at least for the two lowest temperatures. This behavior is most likely due to the fact that crystallization progresses more extensively during the tensile phase, making the material significantly more elastic. This effect is primarily associated with Branch II of the Prony series, which is associated with a very long relaxation time. At 110 °C, the corresponding modulus C_{III} is small, and therefore the residual stress also remains very low.

Below the stress curves, the evolution of the reduced crystallinity factor is plotted on the same time axis. It can be observed that crystallization progresses very little during the tensile stage for the highest strain rates (100 and 200 mm/s), and develops almost exclusively during relaxation. Because crystallization kinetics are slower during this relaxation phase, the stress almost fully relaxes to zero for all temperatures.

Three particular cases should be highlighted, confirming the

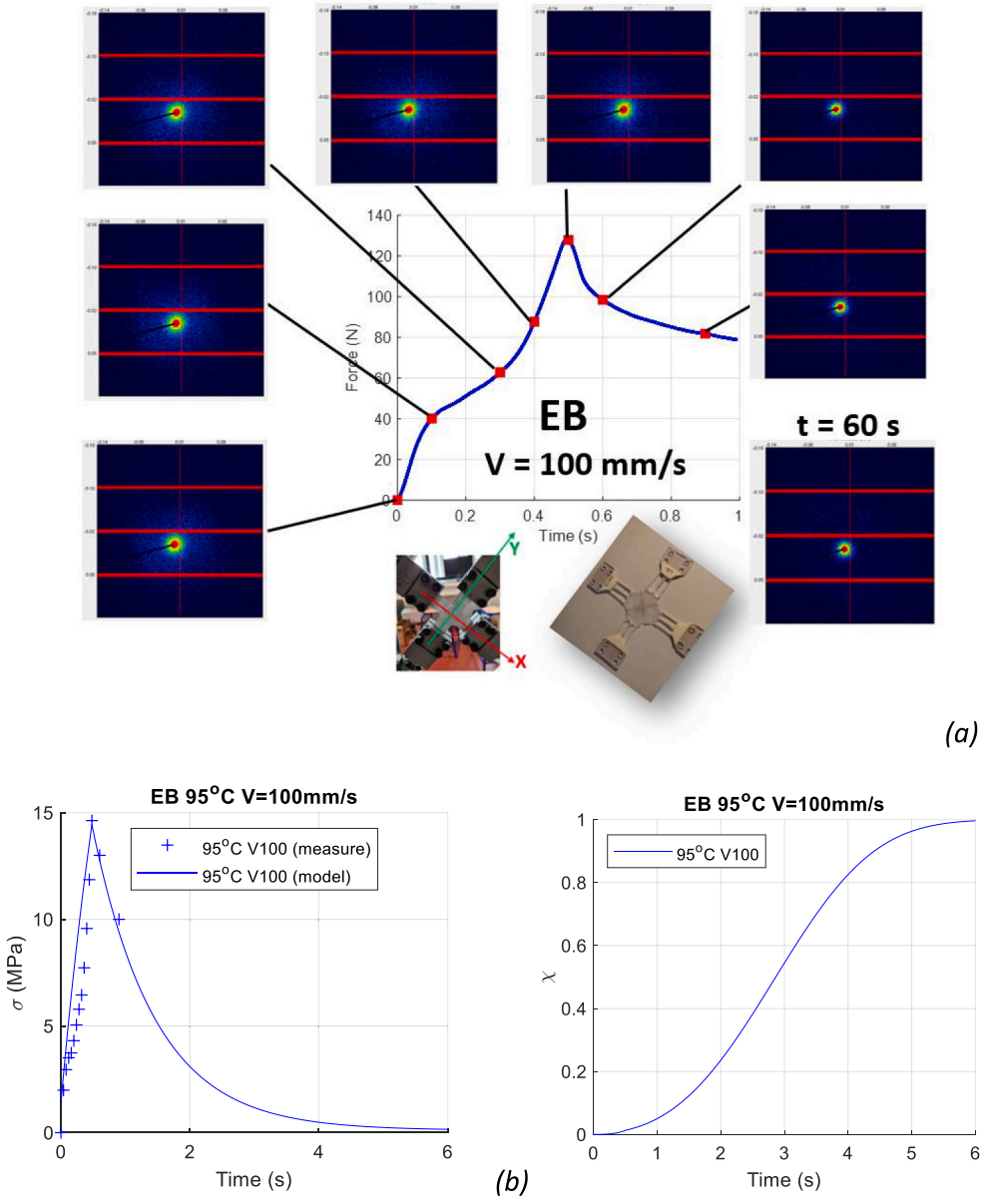

Fig. 12. (a) SAXS measurement during a EB test at 95 °C for a high velocity (V = 100 mm/s); (b) Stress versus time plots for EB test at 95 °C and V = 100 mm/s, as predicted by the DHA-VE model; (c) the corresponding reduced crystallization ratio.

difficulty of reliably interpreting post-mortem crystallinity measurements:

(i) at 100 °C, the highest final crystallinity corresponds to the highest strain rates;
(ii) at 90 °C, the crystallinity curves for 100 and 200 mm/s cross at the end of the tensile stage;
(iii) at 110 °C, the crystallinity curves for 100 and 200 mm/s are almost superimposed.

More precisely, at 90° and 110 °C, the curves obtained at 100 mm/s and 200 mm/s are very close. A clearer distinction between the three cases would likely require an intermediate stretching speed between 25 and 100 mm/s. Nevertheless, a careful examination of the black and blue curves suggests that they are reversed compared to the velocities at 90 °C and nearly identical at 110 °C.

Fig. 11 illustrates the values listed in Table 2, where interpolated values for the case T = 95 °C, corresponding to the test performed under synchrotron radiation, can be clearly visualized. It can be noted that these values are very close to those identified in the previous section, which confirms the consistency of the proposed modeling approach and supports the relevance of the conclusions discussed above. Using these parameters leads to a good representation of the experimental data in the tensile step, the relative error $\frac{1}{N_{\exp}}\sum_{\exp.data}\frac{|\sigma_{sim.}-\sigma_{\exp.}|}{\sigma_{\exp.}}$ computed independently for each temperature set, which remains below 15%.

To complete the validation and the discussion, we consider the additional test shown in Fig. 12. It is an equi-biaxial test carried out at the synchrotron at a higher loading rate. The competition between the characteristic crystallization time and the strain rate is further confirmed, the SAXS images reveal no periodic crystallization on Fig. 12a.

As shown on Fig. 12b using parameter identified in Table 1 leads to a

nice representation of the stress versus time evolution. Fig. 12c shows that the reduced crystallization ratio is only 5% at the end of the biaxial tension and continues to develop during the relaxation phase. But since (i) the test was stopped after 1 s and (ii) the temperature had already begun to decrease, no periodic crystallization could be detected on the images acquired that day, including the one recorded 60 s after unloading.

DSC measurements were performed at ambient temperature on the sample used for the test Fig. 12. It shows that the specimen is also crystalline, 39% in volume, despite not exhibiting a periodic structure. Probably, the rapidity of the test does not allow sufficient time for the macromolecular chains to organize into lamellae during stretching, and crystallization occurs almost entirely during relaxation. At that moment, the material is biaxially stretched and the stretched chains do not have a preferred orientation within the plane. As a result, crystallization occurs in a dispersed manner through a multitude of crystals with an almost cubic geometry, as shown in Refs. [13,14].

5. Conclusions

This work proposes a macroscopic description of PET behavior during equi-biaxial stretching that explicitly couples viscoelasticity and strain-induced crystallization. Starting from an elastic double-homogenization approach, we extended the formulation to the viscoelastic case by using the Laplace–Carson transform and representing the equi-biaxial response with a reduced Prony series. The crystallization kinetics were introduced through an incremental Avrami-type law, in which the coefficient depends on both strain and strain rate.

The model parameters were first identified from an equi-biaxial test performed under synchrotron radiation at 95 °C, for which the microstructure evolution was monitored in situ by SAXS and the final crystallinity was measured by DSC. The same framework was then confronted with a broader series of biaxial tests carried out in the MSME laboratory at 90, 100 and 110 °C and at three stretching velocities. Using a limited number of temperature-dependent parameters, the DHA-VE model reproduces both the strain-hardening behavior and the delayed crystallization occurring mainly during the relaxation phase. The trends obtained for the amorphous modulus, relaxation times and crystallization factor with temperature are consistent with independent identifications, and the overall discrepancy between simulations and experiments remains below about 15 %.

The analysis of the simulated curves also clarifies several features that are difficult to interpret from post-mortem measurements alone, in particular the non-monotonic influence of strain rate on the final crystallinity and the persistence of stresses during relaxation at low stretching speeds. The model thus offers a coherent framework linking process conditions, microstructure development and mechanical response, and can be used as a tool to interpret existing experiments and design new test campaigns.

Future work will focus on extending the approach beyond equi-biaxial loading. Constant-width (CW) tests and non-equi-biaxial (NEB) tests on the same biaxial bench will be particularly useful to probe anisotropic orientation and crystallization. Incorporating explicit descriptors of molecular orientation, together with a refined description of crystalline morphology, should allow us to upgrade the model and move towards a unified prediction of both microstructure and mechanical properties under realistic bottle-blowing conditions.

Declaration of generative AI and AI-assisted technologies in the writing process

During the preparation of this work the authors used *chatgpt* in order to improve the English readability because none of the authors is native English. After using this tool, the authors reviewed and edited the content as needed and take full responsibility for the content of the publication.

CRediT authorship contribution statement

Luc Chevalier: Conceptualization, Formal analysis, Investigation, Methodology, Project administration, Supervision, Validation, Writing – original draft. **Yun-Mei Luo:** Data curation, Formal analysis, Investigation, Methodology, Resources, Software, Validation, Writing – review & editing.

Declaration of competing interest

The authors declare that they have no known competing financial interests or personal relationships that could have appeared to influence the work reported in this paper.

Acknowledgement

The authors gratefully acknowledge the Synchrotron SOLEIL team for the allocated beamtime and for their support during the experiments on the SWING beamline, with special thanks to Javier Perez and Arnaud Gibert. They also thank Benoit Jacquet and Thanh Tung Nguyen for their assistance with SAXS measurements, as well as Evan Gargadennec and Eric Monteiro from PIMM laboratory for complementary DSC measurements and for the development of specific programs related to SAXS data acquisition.

Appendix A. From elastic DHA to viscoelastic DHA, primary consideration

As detailed in Refs. [43,44], we have proposed a framework, illustrated on Fig.A.1, to represent the elastic behavior of PET at ambient temperature after a large biaxial elongation. It consist of a stack of crystalline and amorphous layers, with their respective proportions defined by the crystallinity ratio, α_c.

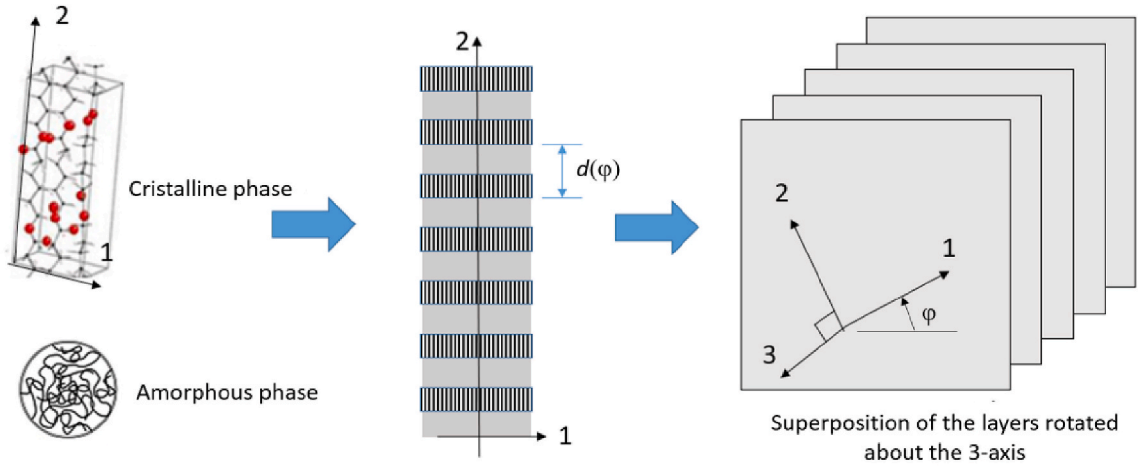

$$d(\varphi) = d_x \cos^2\varphi + d_y \sin^2\varphi$$

Fig. A.1. Two steps homogenization framework.

The analytical formulations assume that the layers are infinite in directions 1 and 3 and are stacked along direction 2. If each phase is transversely isotropic with its axis of symmetry along direction 2, then the resulting multilayer structure is also transversely isotropic about the same axis. Consequently, several components of the elastic stiffness matrix [C] are identical. As a result, only six independent stiffness coefficients C_{ij} need to be determined, instead of nine for a fully orthotropic material. The expressions of components C_{22} (Eq. (A1)), C_{44} and C_{66} (Eq. (A1b)) correspond to mixture laws representing series-type associations of stiffnesses, where the deformations are additive and the compliances (the inverses of stiffnesses) sum up. The effective stiffness in these cases is therefore expressed as:

$$C_{22}{}^{bi} = \frac{1}{\frac{\alpha_c}{C_{22}^c} + \frac{(1-\alpha_c)}{C_{22}^a}} \tag{A1a}$$

$$C_{44}{}^{bi} = C_{66}{}^{bi} = \frac{1}{\frac{\alpha_c}{C_{44}^c} + \frac{(1-\alpha_c)}{C_{44}^a}} \tag{A1b}$$

Conversely, the component C_{55} corresponds to a parallel-type association of the phases, in which the stiffnesses themselves add directly:

$$C_{55}{}^{bi} = \alpha_c C_{55}^c + (1-\alpha_c) C_{55}^a \tag{A2}$$

To explore possible simplifications, it is useful to assess the relative contributions of the various terms in C_{11} or C_{33} (Eq. (A3a)) and C_{13} (Eq. (A3b)) whose full analytical expressions are rather lengthy. By isolating the part corresponding to a series-type association, Fig.A.2 shows that the complementary term is very small compared with the main contribution. Hence, these expressions can be reasonably simplified as follows:

$$C_{11}{}^{bi} = C_{33}{}^{bi} = \alpha_c\left(C_{11}^c - \frac{C_{12}^{c\,2}}{C_{22}^c}\right) + (1-\alpha_c)\left(C_{11}^a - \frac{C_{12}^{a\,2}}{C_{22}^a}\right) + \frac{\left(\alpha_c \frac{C_{12}^c}{C_{22}^c} + (1-\alpha_c)\frac{C_{12}^a}{C_{22}^a}\right)^2}{\frac{\alpha_c}{C_{22}^c} + \frac{(1-\alpha_c)}{C_{22}^a}} \tag{A3a}$$

$$\Rightarrow C_{11}{}^{bi} = C_{33}{}^{bi} \approx \alpha_c C_{11}^c + (1-\alpha_c) C_{11}^a$$

$$C_{13}{}^{bi} = \alpha_c\left(C_{13}^c - \frac{C_{12}^c C_{23}^c}{C_{22}^c}\right) + (1-\alpha_c)\left(C_{13}^a - \frac{C_{12}^a C_{23}^a}{C_{22}^a}\right) + \frac{\left(\alpha_c \frac{C_{12}^c}{C_{22}^c} + (1-\alpha_c)\frac{C_{12}^a}{C_{22}^a}\right)\left(\alpha_c \frac{C_{23}^c}{C_{22}^c} + (1-\alpha_c)\frac{C_{23}^a}{C_{22}^a}\right)}{\frac{\alpha_c}{C_{22}^c} + \frac{(1-\alpha_c)}{C_{22}^a}} \tag{A3b}$$

$$\Rightarrow C_{13}{}^{bi} \approx \alpha_c C_{13}^c + (1-\alpha_c) C_{13}^a$$

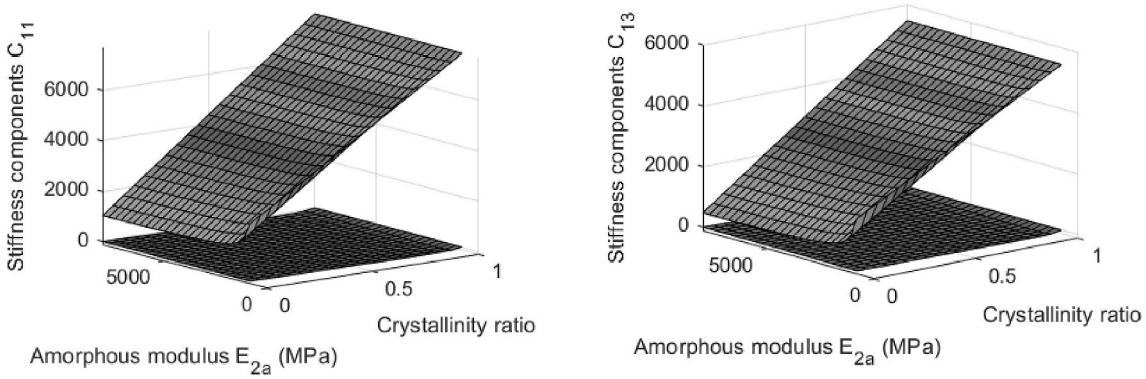

Fig. A.2. Simplification of the components C_{11} and C_{13} of the elastic stiffness tensor [C].

Figure A.2 illustrates the simplifications that can be applied to the components C_{11}^{bi} and C_{13}^{bi}. The inclined surface corresponds to the complete analytical expression, while the nearly flat surface represents the complementary term to the parallel stiffness mixture law. The contribution of these complementary terms is at most 1.83% for C_{11} or C_{33} and 2.64% for C_{13}. Therefore, the proposed simplification is entirely justified. Regarding the remaining component, C_{12}, its expression (Eq. (A4)) does not correspond to either a series-type or a parallel-type mixture law. This is primarily because it involves the term C_{22}, which cannot be isolated in any straightforward manner. Therefore, the exact analytical expression of C_{12} will be retained in the subsequent analysis.

$$C_{12}{}^{bi} = C_{23}{}^{bi} = \frac{\alpha_c \frac{C_{12}^c}{C_{22}^c} + (1-\alpha_c)\frac{C_{12}^a}{C_{22}^a}}{\frac{\alpha_c}{C_{22}^c} + \frac{(1-\alpha_c)}{C_{22}^a}} \tag{A4}$$

Following this first homogenization step, the resulting tensors are rotated, leading to linear expressions. A second homogenization step is then performed on the rotated slices along direction 3. This second step yields either the mean value of the slice components or the mean value of their inverses. The following section describes how each case is treated.

Appendix B. Laplace-Carson transformation to solve a viscoelastic problem

Maxwell Model — Differential and Integral Formulations

The Maxwell model is a representation of viscoelasticity that considers the elastic and viscous phases to be connected in series, such that the overall behavior is more "fluid-like," allowing for possible flow. The classical one-dimensional representation is as follows:

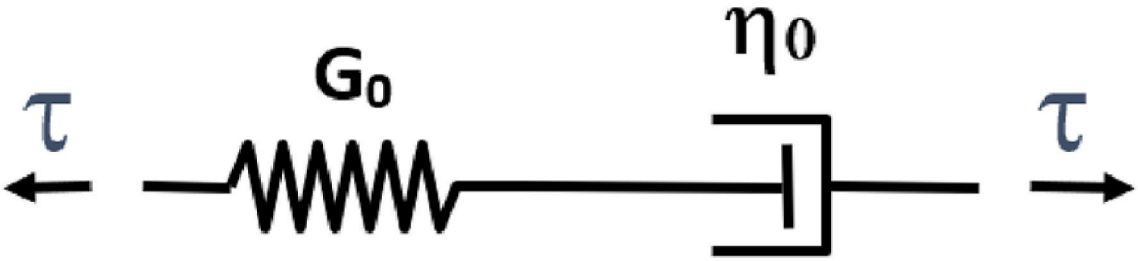

The series combination allows the addition of the elastic and viscous strains or strain rates, which leads to the differential relationship describing shear flow:

$$\tau + \theta\dot{\tau} = \eta_0\dot{\gamma} \;\text{ avec : } \theta = \frac{\eta_0}{G_0} \tag{B1}$$

This law makes it possible to model the phenomena of delayed stress establishment and strain recovery that are observed experimentally. When a step strain γ is applied, the response of the Maxwell model shows a relaxation of the stress τ(t). It can be shown that the expression of the stress is of the form:

$$\tau(t) = G_0 \exp\left(-\frac{t}{\theta}\right)\gamma \tag{B2}$$

By analogy with the elastic law, the relaxation modulus G(t) is defined by the expression Eq. (B3):

$$G(t) = G_0 \exp\left(-\frac{t}{\theta}\right) \tag{B3}$$

The behavior of a polymer is often poorly represented by a single relaxation time. It is therefore necessary to express the relaxation function as an *N*-term Prony series in order to obtain an accurate representation of the material's behavior. In the following, we will continue the developments by considering only a single relaxation time θ, but the entire formulation can be generalized to a multimode model.

Another approach, considered more "intuitive" by rheologists and naturally derived from the relaxation test, consists in viewing the stress as the sum of the strain history through the relation known as the integral formulation:

$$\tau(t) = \int_{-\infty}^{t} G(t-t')\dot{\gamma}(t')dt' \tag{B4}$$

where G(t) is the relaxation function of the form given above. Under these conditions, it is easy to show, by integrating by parts, that the time derivative of the stress leads back to the Maxwell model resulting from the "spring–dashpot" association. Therefore, either of these two formulations can be used for our homogenization process.

Laplace–Carson Transforms

Laplace–Carson transforms are widely used in mechanics because they make it possible to transform a viscoelastic problem in the real (time) domain into a formulation analogous to the same problem in elasticity within the Laplace–Carson space. The Laplace–Carson transform of a function h (t) is defined as:

$$H(p) \text{ ou } \widehat{h}(p) = p\int_{0}^{\infty} h(t)\exp(-pt)dt \tag{B5}$$

where p is a complex variable, and $H(p)$ or $\widehat{h}(p)$ denotes the transform of h(t). This preference over the traditional Laplace transform is justified because the dimensional consistency (and thus the homogeneity) of the equations is preserved during the transformation, unlike with the classical Laplace transform. Below is a table of some common Laplace–Carson transforms:

h(t)	H(p)
$h(t)$	$H(p) = p\int_{0}^{\infty} h(t)\exp(-pt)dt$
$\frac{dh(t)}{dt}$	$pH(p)$
$(h_1{}^*h_2)(t)$	$\frac{H_1(p)H_2(p)}{p}$
A	A
at	$\frac{a}{p}$
t^n	$\frac{n!}{p^n}$
$\exp(-at)$	$\frac{p}{p+a}$
$t\exp(-at)$	$\frac{p}{(p+a)^2}$
$\sin at$	$\frac{ap}{p^2+a^2}$
$\cos at$	$\frac{p^2}{p^2+a^2}$

As a consequence, the transform of the differential formulation can be written as:

$$\tau + \theta\dot{\tau} = \eta_0\dot{\gamma} \Rightarrow \widehat{\tau}(p) = \underbrace{\frac{\eta_0 p}{1+\theta p}}_{\widehat{G}(p)}\widehat{\gamma}(p) \Rightarrow \widehat{G}(p) = \frac{\eta_0}{\theta}\frac{p}{\frac{1}{\theta}+p} = G_0\frac{p}{\frac{1}{\theta}+p} \tag{B6}$$

From the Laplace–Carson transform table (row 7), it can be shown that $\widehat{G}(p)$ is indeed the transform of the relaxation modulus G(t). Likewise, by considering the product $\widehat{G}(p)\times\widehat{\gamma}(p)$ and referring to line 3 of the table, one obtains:

$$\widehat{\tau}(p) = \widehat{G}(p)\times\widehat{\gamma}(p) = \frac{\widehat{G}(p)\times p\widehat{\gamma}(p)}{p} \Rightarrow \tau(t) = \int_{-\infty}^{t} G(t-t')\dot{\gamma}(t')dt' \tag{B7}$$

Data availability

Data will be made available on request.

References

[1] Y.-M. Luo, F. Detrez, L. Chevalier, X. Lu, S. Roland, Multiscale framework for estimation of elastic properties of poly ethylene terephthalate from the crystallization temperature, Mech. Mater. 181 (2023) 104617, https://doi.org/10.1016/j.mechmat.2023.104617.

[2] L. Chevalier, C. Linhone, G. Regnier, Induced crystallinity during stretch–blow moulding process and its influence on mechanical strength of poly(ethylene

terephthalate) bottles, Plast, Rubber Compos. 28 (8) (1999) 393–400, https://doi.org/10.1179/146580199101540556.
[3] N. Anumula, G. Menary, S. Yan, J. Nixon, P. Martin, Processing - property relations from biaxial deformation of PET (polyethylene terephthalate). https://doi.org/10.1063/1.5008075, 2017.
[4] T.T. Nguyen, Y. Luo, L. Chevalier, F. Lesueur, Stochastic simulation of top load test on poly(ethylene terephthalate) bottles: an experimental study on dispersion of elastic properties, J. Appl. Polym. Sci. 138 (34) (2021) 50837, https://doi.org/10.1002/app.50837.
[5] C.W. Tan, G.H. Menary, E.M.A. Harkin-Jones, C.G. Armstrong, P.J. Martin, Effect of biaxial stretching at temperatures and strain histories comparable to injection stretch blow moulding on tensile modulus for polyethylene terephthalate (PET), AIP Conf. Proc. 907 (2007) 835–840, https://doi.org/10.1063/1.2729617.
[6] N. Billon, J.M. Haudin, C. Vallot, C. Babin, Stretch blow moulding of mineral filled PET, Key Eng. Mater. 504–506 (2012) 1099–1104, https://doi.org/10.4028/www.scientific.net/KEM.504-506.1099.
[7] H. Attar, Y.-M. Luo, L. Chevalier, T.T. Nguyen, F. Detrez, Identification of anisotropic properties of polymer sheets from heterogeneous biaxial tests, Polym. Test. 115 (2022) 107721, https://doi.org/10.1016/j.polymertesting.2022.107721.
[8] H.O. Onyishi, C.K. Oluah, Effect of stretch ratio on the induced crystallinity and mechanical properties of biaxially stretched PET, Phase Transitions 93 (9) (2020) 924–934, https://doi.org/10.1080/01411594.2020.1813291.
[9] P. Wawrzyniak, W. Karaszewski, Blowing kinetics, pressure resistance, thermal stability, and relaxation of the amorphous phase of the PET container in the SBM process with hot and cold mold. Part I: research methodology and results, Polymers 12 (8) (2020) 1749, https://doi.org/10.3390/polym12081749.
[10] Y. Bin, K. Oishi, K. Yoshida, M. Matsuo, Mechanical properties of poly(ethylene terephthalate) estimated in terms of orientation distribution of crystallites and amorphous chain segments under simultaneous biaxially stretching, Polym. J. 36 (11) (2004) 888–898, https://doi.org/10.1295/polymj.36.888.
[11] D.C. Prevorsek, P.J. Harget, R.K. Sharma, A.C. Reimschuessel, Nylon 6 fibers: changes in structure between moderate and high draw ratios, J. Macromol. Sci. B 8 (1–2) (1973) 127–156, https://doi.org/10.1080/00222347308245797.
[12] A. Mahendrasingam, C. Martin, W. Fuller, D.J. Blundell, R.J. Oldman, J.L. Harvie, D.H. MacKerron, C. Riekel, P. Engström, Effect of draw ratio and temperature on the strain-induced crystallization of poly (ethylene terephthalate) at fast draw rates, Polymer 40 (20) (1999) 5553–5565, https://doi.org/10.1016/S0032-3861(98)00770-8.
[13] Y. Marco, L. Chevalier, M. Chaouche, WAXD study of induced crystallization and orientation in poly(ethylene terephthalate) during biaxial elongation, Polymer 43 (24) (2002) 6569–6574, https://doi.org/10.1016/S0032-3861(02)00488-3.
[14] Y. Marco, L. Chevalier, M. Chaouche, Cristallisation et orientation induites du PET sous sollicitations biaxiales, Mec. Ind. 5 (4) (2004) 497–505, https://doi.org/10.1051/meca:2004050.
[15] D. Kawakami, S. Ran, C. Burger, C. Avila-Orta, I. Sics, B. Chu, B.S. Hsiao, T. Kikutani, Superstructure evolution in poly(ethylene terephthalate) during uniaxial deformation above glass transition temperature, Macromolecules 39 (8) (2006) 2909–2920, https://doi.org/10.1021/ma052589y.
[16] K. Okada, T. Higashioji, T. Nakagawa, H. Uchida, K. Takahashi, R. Inoue, K. Nishida, T. Kanaya, Structural analysis of poly(ethylene terephthalate) during uniaxial drawing above the glass transition temperature, Polym. J. 45 (1) (2013) 50–56, https://doi.org/10.1038/pj.2012.197.
[17] G. Quandalle, Étude et modélisation mécanique de la cristallisation induite par la déformation des polymères : caoutchouc naturel réticulé et PET, PhD thesis, CEMEF - Centre de Mise en Forme des Matériaux. NNT: 2017PSLEM033, 2017.
[18] P. Mota-Santiago, J. Engqvist, S. Hall, R. Appio, M. Maghe, G. Sathikumar, M. Ristinmaa, T.S. Plivelic, In situ biaxial loading and multi-scale deformation measurements of nanostructured materials at the CoSAXS beamline at MAX IV Laboratory, J. Appl. Crystallogr. 56 (4) (2023) 967–975, https://doi.org/10.1107/S1600576723005034.
[19] J. Zhu, S. Liu, Y. Lu, H. Cheng, X. Han, L. Liu, L. Meng, W. Yu, K. Cui, L. Li, A versatile biaxial stretching device for in situ synchrotron radiation small- and wide-angle x-ray scattering measurements of polymer films, Rev. Sci. Instrum. 94 (2) (2023) 023906, https://doi.org/10.1063/5.0130284.
[20] Q. Zhang, R. Zhang, L. Meng, Y. Lin, X. Chen, X. Li, W. Zhang, L. Li, Biaxial stretch-induced crystallization of poly(ethylene terephthalate) above glass transition temperature: the necessary of chain mobility, Polymer 101 (2016) 15–23, https://doi.org/10.1016/j.polymer.2016.08.054.
[21] W. Zhang, J. Chen, Q. Yan, Q. Zhang, J. Zhao, T. Wu, D. Wang, L. Meng, W. Chen, L. Li, The formation of crystal cross-linked network in sequential biaxial stretching of poly(ethylene terephthalate): the essential role of MD pre-stretch, Polym. Test. 96 (2021) 107143, https://doi.org/10.1016/j.polymertesting.2021.107143.
[22] Y. Lin, W. Chen, L. Meng, D. Wang, L. Li, Recent advances in post-stretching processing of polymer films with in situ synchrotron radiation X-ray scattering, Soft Matter 16 (15) (2020) 3599–3612, https://doi.org/10.1039/C9SM02554E.
[23] N. Billon, Strain induced crystallization of PET under biaxial conditions. From laboratory tests to injection stretch-blow molding, Polymer 277 (2023) 125953, https://doi.org/10.1016/j.polymer.2023.125953.
[24] F.M. Schmidt, J.F. Agassant, M. Bellet, L. Desoutter, Viscoelastic simulation of PET stretch/blow molding process, J. Non-Newtonian Fluid Mech. 64 (1) (1996) 19–42, https://doi.org/10.1016/0377-0257(95)01420-9.
[25] B. Cosson, L. Chevalier, G. Régnier, Simulation of the stretch blow moulding process: from the modelling of the microstructure evolution to the end-use elastic properties of polyethylene terephthalate bottles, Int. J. Material Form. 5 (1) (2012) 39–53, https://doi.org/10.1007/s12289-010-1010-y.
[26] L. Chevalier, Y.M. Luo, E. Monteiro, G.H. Menary, On visco-elastic modelling of polyethylene terephthalate behaviour during multiaxial elongations slightly over the glass transition temperature, Mech. Mater. 52 (2012) 103–116, https://doi.org/10.1016/j.mechmat.2012.05.003.
[27] Y.M. Luo, L. Chevalier, F. Utheza, X. Nicolas, Simplified modelling of the infrared heating involving the air convection effect before the injection stretch blowing moulding of PET preform, Key Eng. Mater. 611–612 (2014) 844–851, https://doi.org/10.4028/www.scientific.net/KEM.611-612.844.
[28] Y. Luo, L. Chevalier, E. Monteiro, S. Yan, G. Menary, Simulation of the injection stretch blow molding process: an anisotropic visco-hyperelastic model for polyethylene terephthalate behavior, Polym. Eng. Sci. 60 (4) (2020) 823–831, https://doi.org/10.1002/pen.25341.
[29] Y.-M. Luo, L. Chevalier, E. Monteiro, F. Utheza, Numerical simulation of self heating during stretch blow moulding of PET: viscohyperelastic modelling versus experimental results, Int. J. Material Form. 14 (4) (2021) 703–714, https://doi.org/10.1007/s12289-020-01565-w.
[30] C. Buckley, Glass-rubber constitutive model for amorphous polymers near the glass transition, Polymer 36 (17) (1995) 3301–3312, https://doi.org/10.1016/0032-3861(95)99429-X.
[31] X.-T. Pham, F. Thibault, L. Lim, Modeling and simulation of stretch blow molding of polyethylene terephthalate, Polym. Eng. Sci. 44 (8) (2004) 1460–1472, https://doi.org/10.1002/pen.20142.
[32] H. Mir, Z. Benrabah, F. Thibault, The use of elasto-visco-plastic material model coupled with pressure-volume thermodynamic relationship to simulate the stretch blow molding of polyethylene terephthalate, AIP Conf. Proc. 908 (2007) 331–336, https://doi.org/10.1063/1.2740833.
[33] G. Marckmann, E. Verron, B. Peseux, Finite element analysis of blow molding and thermoforming using a dynamic explicit procedure, Polym. Eng. Sci. 41 (3) (2001) 426–439, https://doi.org/10.1002/pen.10740.
[34] S. Yan, G. Menary, J. Nixon, A novel methodology to characterize the constitutive behaviour of polyethylene terephthalate for the stretch blow moulding process, Mech. Mater. 104 (2017) 93–106, https://doi.org/10.1016/j.mechmat.2016.10.006.
[35] J. Nixon, G.H. Menary, S. Yan, Finite element simulations of stretch-blow moulding with experimental validation over a broad process window, Int. J. Material Form. 10 (5) (2017) 793–809, https://doi.org/10.1007/s12289-016-1320-9.
[36] F. Teng, G. Menary, S. Yan, J. Nixon, J.B. Stevens, A hybrid artificial neural network approach for modeling the behavior of polyethylene terephthalate (PET) under conditions applicable to stretch blow molding, Polymers 17 (8) (2025) 1067, https://doi.org/10.3390/polym17081067.
[37] M.-C. Reuvers, B. Boes, S. Felder, T. Brepols, S. Kulkarni, K. Loos, M. Johlitz, A. Lion, S. Reese, Semi-crystalline polymers at finite strains: a thermo-coupled constitutive model for varying degrees of crystallinity and temperatures, Proc. Appl. Math. Mech. 23 (1) (2023) e202200162, https://doi.org/10.1002/pamm.202200162.
[38] M.-C. Reuvers, S. Kulkarni, B. Boes, S. Felder, A. Wutzler, M. Johlitz, A. Lion, T. Brepols, S. Reese, A thermo-mechanically coupled constitutive model for semi-crystalline polymers at finite strains: mechanical and thermal characterization of polyamide 6 blends, Continuum Mech. Therm. 36 (3) (2024) 657–698, https://doi.org/10.1007/s00161-024-01288-2.
[39] S.-R. Merouani, R. Hosseinnezhad, Z. Yan, F. Zaïri, I. Vozniak, Multiphase constitutive modeling for interphase-driven mechanics in polymer blends: application to PE/PS and PP/PS systems processed by solid-state and melt mixing, Int. J. Solid Struct. 324 (2026) 113666, https://doi.org/10.1016/j.ijsolstr.2025.113666.
[40] T. Nan, Y. Chen, W. Liu, C. Zhang, A finite strain viscoelastic–viscoplastic damage model for thermoplastic polymer, Appl. Math. Model. 146 (2025) 116180, https://doi.org/10.1016/j.apm.2025.116180.
[41] U.K. Jinaga, K. Zulueta, A. Burgoa, L. Cobian, U. Freitas, M. Lackner, Z. Major, L. Noels, A consistent finite-strain thermomechanical quasi-nonlinear-viscoelastic viscoplastic constitutive model for thermoplastic polymers, Int. J. Solid Struct. 321 (2025) 113517, https://doi.org/10.1016/j.ijsolstr.2025.113517.
[42] Y.-M. Luo, T.T. Nguyen, H. Attar, L. Chevalier, F. Lesueur, A new biaxial apparatus for tensile tests on Poly Ethylene Terephthalate optimized specimen at stretch blow molding conditions, Polym. Test. 113 (2022) 107676, https://doi.org/10.1016/j.polymertesting.2022.107676.
[43] L. Chevalier, Y.-M. Luo, T.T. Nguyen, H. Attar, Multiscale framework for estimation of induced elastic properties of poly ethylene terephthalate after biaxial elongation, Mech. Mater. 192 (2024) 104962, https://doi.org/10.1016/j.mechmat.2024.104962.
[44] T.T. Nguyen, Y.-M. Luo, L. Chevalier, Morphology evolution in biaxially stretched polyethylene terephthalate and prediction of final elastic properties, Polym. Test. 150 (2025) 108929, https://doi.org/10.1016/j.polymertesting.2025.108929.
[45] W.H. Peters, W.F. Ranson, Digital imaging techniques in experimental stress analysis, Opt. Eng. 21 (3) (1982), https://doi.org/10.1117/12.7972925.
[46] M.A. Sutton, J.-J. Orteu, H.W. Schreier, Image Correlation for Shape, Motion and Deformation Measurements: Basic Concepts, Theory and Applications, Springer, 2009.
[47] C. Caggegi, L. Chevalier, V. Pensée, M. Cuomo, Strain and shear stress fields analysis by means of Digital Image Correlation on CFRP to brick bonded joints fastened by fiber anchors, Constr. Build. Mater. 106 (2016) 78–88, https://doi.org/10.1016/j.conbuildmat.2015.12.089.
[48] M. Quanjin, M.R.M. Rejab, Q. Halim, M.N.M. Merzuki, M.A.H. Darus, Experimental investigation of the tensile test using digital image correlation (DIC) method, Mater. Today Proc. 27 (2020) 757–763, https://doi.org/10.1016/j.matpr.2019.12.072.

[49] J. Nixon, G. Menary, Determining volumetric strain in biaxial deformation of PET at temperatures and strain rates for stretch blow moulding, Key Eng. Mater. 651–653 (2015) 869–873, https://doi.org/10.4028/www.scientific.net/KEM.651-653.869.
[50] M. Avrami, Kinetics of phase change. I general theory, J. Chem. Phys. 7 (12) (1939) 1103–1112, https://doi.org/10.1063/1.1750380.
[51] M. Avrami, Kinetics of phase change. II transformation-time relations for random distribution of nuclei, J. Chem. Phys. 8 (2) (1940) 212–224, https://doi.org/10.1063/1.1750631.
[52] M. Avrami, Granulation, phase change, and microstructure kinetics of phase change. III, J. Chem. Phys. 9 (2) (1941) 177–184, https://doi.org/10.1063/1.1750872.
[53] K. Nakamura, T. Watanabe, K. Katayama, T. Amano, Some aspects of nonisothermal crystallization of polymers. I. Relationship between crystallization temperature, crystallinity, and cooling conditions, J. Appl. Polym. Sci. 16 (5) (1972) 1077–1091, https://doi.org/10.1002/app.1972.070160503.
[54] C.A. Hieber, Correlations for the quiescent crystallization kinetics of isotactic polypropylene and poly(ethylene terephthalate), Polymer 36 (7) (1995) 1455–1467, https://doi.org/10.1016/0032-3861(95)95925-Q.
[55] J.A. Pople, G.R. Mitchell, S.J. Sutton, A.S. Vaughan, C.K. Chai, The development of organized structures in polyethylene crystallized from a sheared melt, analyzed by WAXS and TEM, Polymer 40 (10) (1999) 2769–2777, https://doi.org/10.1016/S0032-3861(98)00202-X.
[56] A. Poitou, A. Ammar, Y. Marco, L. Chevalier, M. Chaouche, Crystallization of polymers under strain: from molecular properties to macroscopic models, Comput. Methods Appl. Mech. Eng. 192 (28–30) (2003) 3245–3264, https://doi.org/10.1016/S0045-7825(03)00349-9.
[57] M.L. Di Lorenzo, Crystallization of poly(ethylene terephthalate): a Review, Polymers 16 (14) (2024) 1975, https://doi.org/10.3390/polym16141975.
[58] Y. Gong, F. Detrez, Y. Luo, L. Chevalier, Simulation of microstructure evolution for polymer using the phase field method: crystallization induced by temperature, Polymer Crystallization 2 (6) (2019), https://doi.org/10.1002/pcr2.10091.
[59] M. Matsuo, C. Sawatari, Elastic modulus of polyethylene in the crystal chain direction as measured by x-ray diffraction, Macromolecules 19 (7) (1986) 2036–2040, https://doi.org/10.1021/ma00161a042.